Experimental and Numerical study of Macro-cell Corrosion between Crossed Steel Bars

Z. Dong, X.L. Gu and Z.H. Jin

Key Laboratory of Performance Evolution and Control for Engineering Structures, Ministry of Education
College of Civil Engineering, Tongji University, Shanghai, China

ABSTRACT

Reinforcing steel bars embedded in concrete are always intersected with each other to form rebar mesh or three-dimensional steel cage. The present study aims to investigate the phenomenon of severe corrosion observed at stirrups or some intersections of steel rebar mesh, which has not been well studied before. Macro-cell corrosion between crossed steel bars was considered to be the major cause for this phenomenon. In this regard, crossed steel bars were divided into intersected zone (IZ) and non-intersected zone (NIZ). The macro-cell current at the face-to-face IZ was calculated by Ohm's law. A one-dimensional model based on transmission line method was employed to obtain the distribution of macro-cell current on the NIZ juxtaposed to the IZ. Experiments of steel bars in aqueous solutions and concrete were undertaken to verify the numerical model. The results demonstrated a good match between experiments and numerical model. It was also shown that the distribution of macro-cell current on the non-intersected areas was influenced by the resistivity of electrolyte. Based on the corrosion rate model presented in this study, the severe corrosion observed at stirrups or some intersection zones of rebar mesh can be explained and quantified.

Keywords: Corrosion rate, crossed steel bars, macro-cell corrosion, transmission line.

1.   INTRODUCTION

Corrosion of steel bars is one of the main causes for the deterioration of mechanical behavior of reinforced concrete (RC) structures under marine atmospheric environment (Lewis and Copenhagen W J., 1959; DuraCrete, 2000; Pech-Canul and Castro, 2002). Researchers have conducted studies with respect to the corrosion mechanisms (Andrade *et al.*, 1992; Hansson, Poursaee and Laurent, 2006; Ji *et al.*, 2013; Hornbostel *et al.*, 2016), corrosion morphology (Ji *et al.*, 2013; Angst *et al.*, 2017) and environmental effects on corrosion (Huet *et al.*, 2007). As fundamentally known, microcell and macro-cell corrosion both can occur on the surface of steel embedded in concrete exposed to chloride

a RC structure, macro-cell can be formed between dissimilar steel bars with different potentials due to 1) chloride concentration gradients during the penetration process and 2) material differences between steel bars. It should be noted that unlike the simplified view of "active steel becoming anode and passive steel cathode" in pitting corrosion, in the macro-cell corrosion between different steel bars, the anodic dissolution of iron and cathodic reduction of oxygen occur on the surfaces of both steel surfaces. Examples of this situation can be the severe corrosion observed at stirrups (Fu *et al.*, 2017) or some intersection points of reinforcements

(Alhozaimy *et al.*, 2012), and active steel in contact with a bottom steel in chloride-free concrete (Hansson, Poursaee and Laurent, 2006). In these cases, the corrosion of steel with more negative potential can be aggravated under the coupled micro- and macro-cell corrosion process, which may further lead to the reduction in its sectional area and the structural reliability. Prediction models of corrosion rate including theoretical model (Bazant, 1979a, 1979b), empirical model considering factors like crack (Otieno, Beushausen and Alexander, 2016), temperature and chloride content (Liu and Weyers, 1998), and semi-empirical model based on limiting step (Guidelines and Design, 2000) have been proposed. However, this macro-cell corrosion has not been sufficiently studied and taken into account in ___ates because of the ___ corrosion process.

The present study focused on the macro-cell formed between crossed steel bars like the stirrups and corresponding main rebar. As shown in Fig.1, when a RC structure is subjected to chloride ingress, steel bar which is placed near the concrete surface (cf. Fig. 1, steel 1) may be depassivated earlier than the connected inner bar (cf. Fig.1, steel 2). Consequently, the potential of the corroding steel 1 is more negative than that of steel 2, leading to the formation of macro-cell. With the ongoing penetration process of chloride ions, steel 2 may start to corrode afterwards. Macro-cell between steel 1 and steel 2 may diminish.

However, since the concentration of chloride ions is generally lower in deeper depth (Pack *et al.*, 2010), steel 1 could still possess a more negative potential than steel 2 (Fu *et al.*, 2017). This is due to the more negative potential of metal with increased concentration of chloride ions (Altun and Sen, 2004; Izquierdo *et al.*, 2004; Moreno *et al.*, 2004).
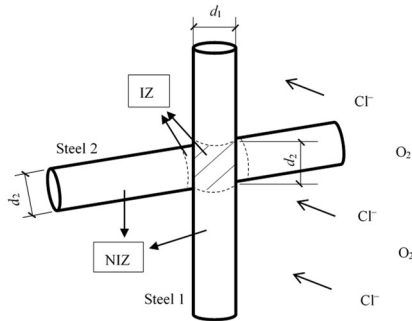

Fig. 1. Crossed steel bars being divided into IZ (diagonal hatching) and juxtaposed NIZ (Steel 1 is placed near the concrete surface, while steel 2 is the inner bar contacted with steel 1)

As the crossed steel electrodes can not be simply categorized into face-to-face or coplanar electrodes, this study divided the crossed reinforcement into intersected zone (IZ) and non-intersected zone (NIZ) (cf. Fig. 1). The macro-cell current at the face-to-face IZ was calculated by Ohm's law. A one-dimensional model based on transmission line method (Tahara and Kodama, 2000; Song, 2010) was employed to obtain the distribution of macro-cell current on the juxtaposed NIZ.

2. THEORETIC MODEL

2.1 Macro-cell Current at IZ

The dimensions of IZ are considered to be the corresponding diameters of crossed steel bars (cf. diagonal hatching in Fig. 1). As such, the type of macro-cell at IZ can be regarded as the face-to-face electrodes with an area ratio of one. The corresponding macro-cell current can thus be calculated through Ohm's law, as expressed in the following equation:

$$I_g = \frac{\Delta E_{corr}}{R} = \frac{E_{corr2} - E_{corr1}}{R} = \frac{E_{corr2} - E_{corr1}}{P_1 + P_2 + R_{con}} \quad (1)$$

where ΔE_{corr} is the potential difference between steel 1 (E_{corr1}) and steel 2 (E_{corr2}), P_1 and P_2 are the polarization resistance of steel 1 and steel 2, R_{con} is the corresponding concrete resistance.

Since the surrounding concrete is contaminated with chloride ions under chloride environments, the concrete resistance between IZ may not be taken into account. This is due to the inverse proportional relationship between chloride concentration and electrical concrete resistivity. For the sake of application, the polarization resistance of steel is transformed to the polarization resistivity ρ_p ($\Omega \cdot m^2$), which can be calculated by Eq. (2). Thus, the corresponding macro-cell current density (i.e. the ratio of macro-cell current to the surface area of steel 1 at IZ) can be expressed as Eq. (4).

$$\rho_p = \frac{\Delta E}{\Delta i} \quad (2)$$

$$\frac{A_1}{A_2} = \frac{\pi \cdot d_1 \cdot d_2}{\pi \cdot d_2 \cdot d_1} = 1 \quad (3)$$

$$i_g = \frac{I_g}{A_1} = \frac{\Delta E_{corr}}{\rho_{p1} + \rho_{p2} \cdot \frac{A_1}{A_2}} = \frac{\Delta E_{corr}}{\rho_{p1} + \rho_{p2}} \quad (4)$$

where ΔE is the polarization value, Δi is the corresponding current density, d_1 and d_2 are the diameters of steel 1 and steel 2, A_1 and A_2 are the surface areas of steel 1 and steel 2 at the IZ.

The above Ohm's law was fundamentally known and applied to calculate the macro-cell current between face-to-face steel electrodes (Andrade *et al.*, 1992).

2.2 Distribution of Macro-cell Current at NIZ

As for the steel 1 which possesses more negative potential than steel 2 under chloride ingress (cf. Fig. 1), when it is coupled to steel 2, the potential at its IZ is considered to be varied ahead of juxtaposed NIZ. Thus, a potential difference is generated between the surfaces of IZ and NIZ. The corresponding potential difference at the boundary of IZ and NIZ is regarded as the initial value (η_0). For the symmetrical half part of NIZ, it is assumed that the distribution of potential difference (or polarization value) over the unit steel section is gradually decreased, as the curve plotted in Fig. 2. Under such potential difference, the steel surfaces at different position of NIZ will be anodically polarized to different degrees. R_s and P are the electrolyte resistance and polarization resistance of unit length, which are simplified to be constants in this study. The resistance of electron in steel is ignored due to its sufficient electrical conductivity.
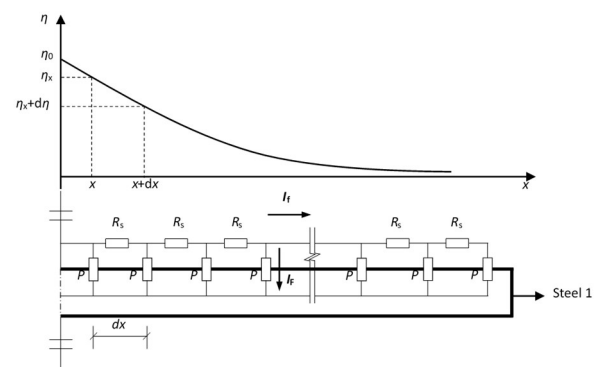

Fig. 2. Schematic illustration of NIZ of steel 1 and corresponding potential difference distribution (η_x)

The potential difference (η_x) along the steel surface generates non-faradic current (I_t) and faradic current (I_F). The direction of the former is parallel to the steel-concrete interface, while the direction of the latter is perpendicular to the steel-concrete interface.

The distribution of potential difference (η_x) can be derived as (Tahara and Kodama, 2000; Song, 2010) (see Appendix A):

$$\eta_x = A \cdot \exp\left(\frac{x}{\xi}\right) + B \cdot \exp\left(-\frac{x}{\xi}\right) \qquad (5)$$

where A and B are the constants which need to be determined by boundary conditions, ξ can be expressed as Eq. (6).

$$\xi = \sqrt{\frac{\rho_p \cdot c}{\rho_s}} \qquad (6)$$

where ρ_p and ρ_s are the polarization resistivity and electrolyte resistivity; c is the cover depth.

As mentioned above, the potential difference at the boundary of IZ and NIZ equals to the initial value (η_0) (cf. Eq. (7)). Meanwhile, the flowing current I_f at the end of steel 1 should be zero (cf. Eq. (8)).

$$\eta|_{x=0} = \eta_0 \qquad (7)$$

$$I_f|_{x=L} = 0 \quad \text{i.e.} \quad \left.\frac{d\eta_x}{dx}\right|_{x=L} = 0 \qquad (8)$$

where L is the symmetrical half length of NIZ.

With these boundary conditions, the following equations of the one-dimensional circuit system can be deduced:

$$\eta_x = \frac{\eta_0 \cdot \cosh\left(\dfrac{x-L}{\xi}\right)}{\cosh\left(\dfrac{L}{\xi}\right)} \qquad (9)$$

$$I_F = -\frac{\eta_x}{\rho_{p1}} = -\frac{\eta_0 \cdot \cosh\left(\dfrac{x-L}{\xi}\right)}{\rho_{p1} \cdot \cosh\left(\dfrac{L}{\xi}\right)} \qquad (10)$$

where ρ_{p1} is the one-dimensional polarization resistivity of steel (cf. Eq. (A.2)).

2.3 Corrosion Rate of Steel under Coupled Micro- and Macro-cell Corrosion Process

Once the steel is under the coupled micro- and macro-cell corrosion process, its potential will be deviated from the free potential, as well as the corresponding anodic and cathodic currents. The potential of the steel with more negative free potential (E_{corr1}) will be shifted to a less negative potential, while the steel with more positive free potential (E_{corr2}) will be shifted in the opposite direction. As shown in Fig. 3, the potential of steel 1 (cf. Fig. 1) shifts from E_{corr1} to E_1, while the anodic dissolution current moves from I_{corr1} to I_{a1}. The increased anodic dissolution current (ΔI_{corr1}) is smaller than the magnitude of the macro-cell current (I_g), since part of I_g needs to compensate for the decrease in the corresponding cathodic current ($\Delta I'_{corr1}$). As such, the anodic current of steel 1 under coupled micro- and macro-cell corrosion is the sum of corrosion current (I_{corr1}) and the increased anodic dissolution current (ΔI_{corr1}):

$$I_{a1} = I_{corr1} + \Delta I_{corr1} \qquad (11)$$
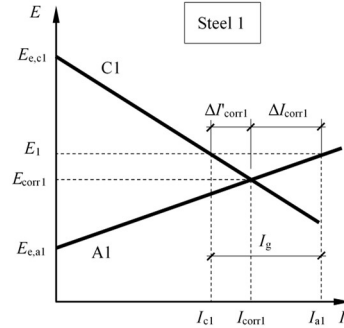

Fig. 3. Linear E-I relationship for coupled micro- and macro-cell corrosion of an actively corroding steel (cf. Fig. 1, steel 1)

The proportion of ΔI_{corr1} to I_g can approximately equal to 60% (Laidler, 1970; Qian, Zhang and Qu, 2006), which is calculated from the obtained Tafel slopes. Accordingly, the anodic dissolution current of steel 1 (cf. Fig. 1) at IZ and NIZ can be obtained:

$$\begin{cases} I_{a1} = I_{corr1} + 0.6 \cdot I_g, & \text{intersected zone} \\ I_{a1} = I_{corr1} + 0.6 \cdot I_F, & \text{non-intersected zone} \end{cases} \qquad (12)$$

3. EXPERIMENTAL STUDY

To investigate the distribution of macro-cell current between IZ and NIZ, corrosion tests were carried out in solutions and concrete.
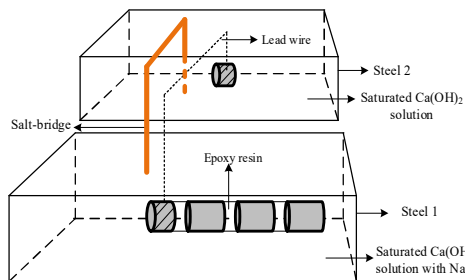
3.1 Corrosion tests in solution

The steel electrodes were segments with different lengths machined from an identical mild steel bar (HPB300). As illustrated in Figs. 4 and 5, the steel segments with 10 mm-length simulated the IZ, while the steel segments with 30mm-length simulated the NIZ. The diameters of all the steel segments were 10 mm. As such, the area ratio of steel 1 to steel 2 at the simulated IZ was kept as one. Conductive wires were welded to the end of each steel segment, epoxy resin was then employed to isolated each steel electrode. Ahead of corrosion tests, all the steel segments were immersed into a simulated pore solution (pH=13.60) for one week, ensuring the passive state of steel bars before getting corroded. The composition of the pore solution is listed in Table 1.

The corrosion tests were carried out in saturated calcium hydroxide (Ca(OH)$_2$) solution with or without 0.05 mol/L NaCl. Segments of steel 1 were put into the former to induce corrosion, while the steel 2 was put into the latter to keep the passive state (cf. Fig. 4).

Table 1. Composition of simulated pore solution (pH=13.60)

Chemical composition	NaOH	KOH	Ca(OH)$_2$
Content (g/L)	8.33	23.30	2.00

Fig. 4. Test set-up for corrosion of steel bars in solution
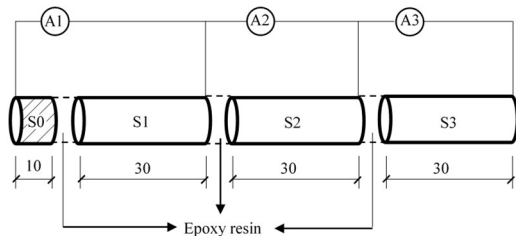
Fig. 5. Measurement of macro-cell current between steel segments (mm)

Once the segments of steel 1 were monitored to be in the active state by corrosion potential, they were put into aqueous solutions of different resistivity, as listed in Table 2. The height of solution above on the steel was kept as 16 mm. The corrosion potentials of corroding steel segments were measured relative to a silver/silver chloride reference electrode (SSCE). Zero resistance ammeter was used to measure the macro-cell current, as illustrated in Fig. 5.

It should be noted that the chloride ions were inevitably transported from the solution with NaCl to the other through the salt-bridge, leading to the occurrence of a mild corrosion on the surface of steel 2. Nevertheless, the corrosion potential of steel 2 was monitored to be still less negative than that of the segments of steel 1, due to an obviously low chloride concentration.

Table 2. Values of conductivity and resistivity of the electrolytes used

Electrolyte	Conductivity (S·m^{-1})	Resistivity (Ω·m)
Deionized water (DW)	3.99×10^{-4}	2506.26
Tap water (TW)	1.78×10^{-2}	56.18

3.2 Corrosion tests in concrete

In addition to the above experiments in solutions, macro-cell current measurements were carried out on steel segments embedded in concrete specimen. The steel segments were machined from the same mild steel bar, while the length of S1~3 (cf. Fig. 6) was 25 mm. Due to the inhomogeneity of concrete, the corrosion potentials and corresponding corrosion rates of segments S1~3 (S1'~3') were inevitably not as similar as that in the aqueous solutions. Therefore, the stainless steel (SS) was used as the coupled passive steel to ensure a considerable initial potential difference between simulated IZ and NIZ. The dimensions of concrete specimen were 280 mm×125 mm×100 mm. Distribution of macro-cell current was measured as illustrated in Fig. 7. The composition of the concrete mixtures, the compressive strength of prismatic specimens and the bulk resistivity of cylinder specimens are listed in Table 3.
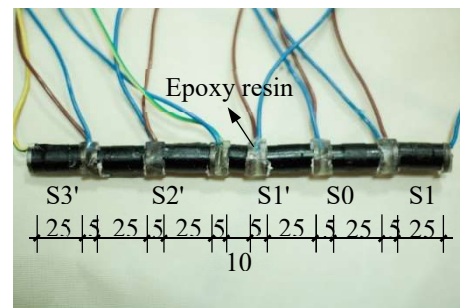
Fig. 6. Steel segments joined with epoxy resin (mm)
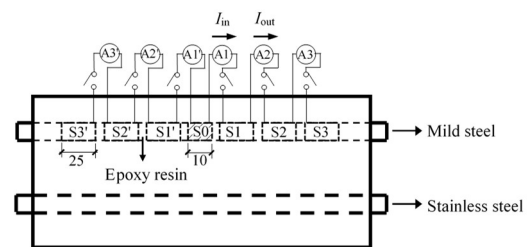
Fig. 7. Schematic illustration of steel segments in concrete specimen (mm)

Table 3. Composition and physical properties of concrete specimens

	Cement #425 (kg/m^3)	154
	Water (kg/m^3)	185
Composition	Fine aggregate (kg/m^3)	650
	Coarse aggregate (kg/m^3)	1207
	Ground granulated blastfurnace slag (GGBS) (kg/m^3)	154
Physical properties	28-day compressive strength (MPa)	24.3
	28-day electrical resistivity (Ω·m)	1241.6

The concrete specimens were cured in a 95 ± 5% relative humidity (RH) and 20 ± 2 °C environment for 28 days, and were then put in a chamber with salt

spray nozzles to induce corrosion. The temperature was kept as 25 °C. The macro-cell current was measured through ammeter, and the current value of each steel segment was calculated through Eq. (13). An average value of the bilateral symmetrical measured macro-cell currents and corrosion potentials were used in the analysis.

$$I_g = I_{out} - I_{in} \qquad (13)$$

where I_{out} is the outflow current from the steel segment, and I_{in} is the inflow current to the steel (cf. Fig. 7).

4. RESULTS AND DISCUSSION

The potentials of active steel segments S0 in aqueous solutions and concrete before and after being connected to the other steel with less negative potential are listed in Table 4. The segment S0 in aqueous solutions was connected to steel 2 through wires and salt-bridge, while in concrete it was connected to the stainless steel (SS) through wires. In all cases, the potentials of S0 after connection were more positive than before as a result. The SS beneath the mild steel in concrete specimens performed a way less negative potential than mild steel. Thus, in concrete specimen, the potential of S0 was observably more positive after being coupled with SS than before.

Based on the concrete resistance measured through electrochemical impedance spectroscopy (EIS), the electrical concrete resistivity at the time of macro-cell current measurements was calculate through the following equation:

$$\rho_s = R_s \cdot k \qquad (14)$$

where ρ_s is the bulk resistivity of concrete specimens, R_s is the concrete resistance measured through EIS, k is the cell constant calculated through the 28-day bulk resisitivity ($\rho_{s,28}$) and corresponding concrete resistance ($R_{s,28}$) measured by EIS (cf. Eq. (15)).

$$k = \frac{\rho_{s,28}}{R_{s,28}} \qquad (15)$$

The polarization resistivity of steel segment (ρ_p) was obtained by linear polarization resistance (LPR) measurement through a three electrodes system. The

measured value of macro-cell currents (I_g) and corresponding predicted results through Eq. (10) in section 2.2 were shown in Fig. 8.

As Fig. 8 shows, though there existed some deviations, the predicted results of macro-cell currents indicated a reasonable agreement with the measured results. According to Eq. (10) in section 2.2, different initial potential difference (η_0) on the boundary of IZ and NIZ will obviously result in different magnitudes of corresponding macro-cell current distributed on the surfaces of NIZ. Therefore, to compare the macro-cell current induced by unit η_0 under dissimilar electrolyte resistivities, the ratio of I_g to corresponding η_0 was set as the ordinate (cf. Fig. 9). In the present study, the tap water (TW) possessed the lowest electrical resistivity, while the deionized water (DW) the highest among three electrolytes. According to Eq. (10), high electrical resistivity leads to a low value of distributed macro-cell current, while keeping other parameters as constants. This was validated by the experimental results (cf. Fig. 8). However, since the corrosion potential of each steel segment in electrolytes of different resistivity was more or less dissimilar, it was hard to merely vary the electrical resistivity while keep other parameters constant. This may be the reason that the observed regulation from measured I_g were not entirely in accord with prediction. For instance, the macro-current of segments in DW was somewhat higher than that in concrete in the distance of ca. 4~6 cm (cf. Fig. 9).

Table 4. Values of potentials of steel segments

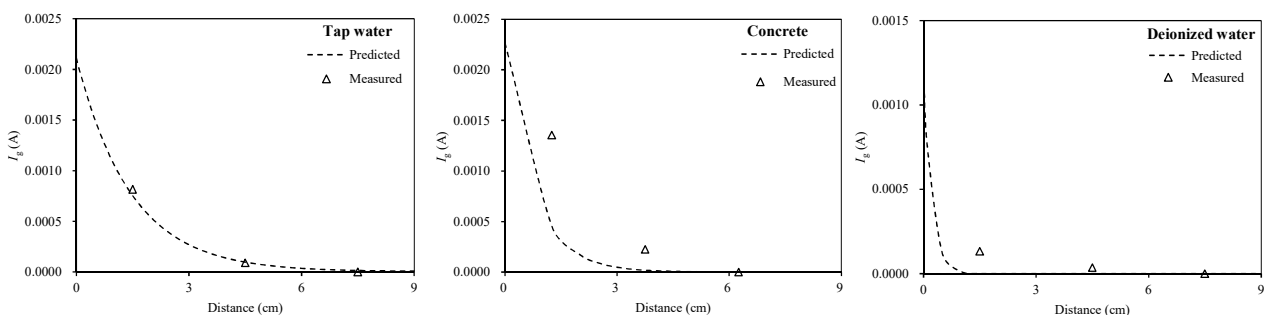|	Segment	S0
Potential before connection (V, SSCE)	In aqueous solutions	−0.57
	In concrete	-0.51
Potential after connection (V, SSCE)	In aqueous solution (DW)	-0.54
	In aqueous solution (TW)	-0.52
	In concrete	-0.38

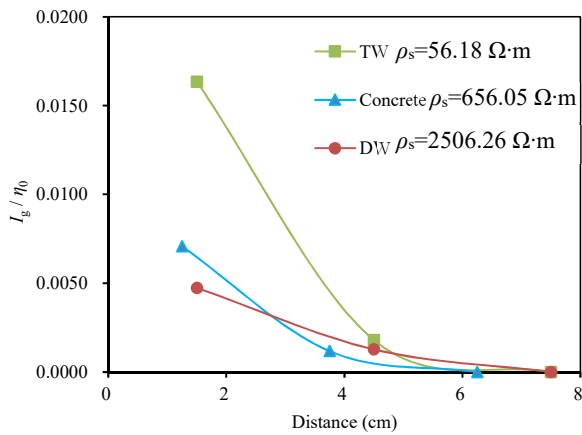**Fig. 8.** Predicted and measured macro-cell currents

Fig. 9. Values of I_g/η_0 versus distance in electrolytes of different electrical resistivity.

5. CONCLUSIONS

The present study dealt with the macro-cell corrosion between crossed steel macro-couples by dividing the steel bar into intersected zone (IZ) and non-intersected zone (NIZ). A one-dimensional model to calculate the macro-cell current of crossed steel reinforcement was developed based on transmission line method. By combining the experimental results with the predicted results, it was validated that the value of macro-cell current distributed on the NIZ of crossed steel bars was inversely proportional to the electrolyte resistivity. It is implied that, as to crossed steel bars, a low electrical concrete resistivity will not only be correlated to a possible high corrosion rate of steel, but also can lead to a high macro-cell current on the NIZ. In this regard, the corrosion of the steel with more negative free potential will be further aggravated under the coupled micro- and macro-cell corrosion process, especially in concrete with high resistivity. To comprehensively analyze the macro-cell of crossed steel, other factors like the geometry will be further investigated.

Acknowledgement

Appendix A

Applying the transmission line method (Tahara and Kodama, 2000; Song, 2010) to the scenario of crossed steel reinforcements embedded in concrete. The one-dimensional electrolyte resistivity of concrete ρ_{s1} and corresponding polarization resistivity of steel ρ_{p1} can be expressed as:

$$\rho_{s1}\ [\Omega/\mathrm{m}] = \frac{\rho_s\ [\Omega \cdot \mathrm{m}]}{\pi \cdot d \cdot c\ [\mathrm{m}^2]} \tag{A.1}$$

$$\rho_{p1}\ [\Omega \cdot \mathrm{m}] = \frac{\rho_p\ [\Omega \cdot \mathrm{m}^2]}{\pi \cdot d\ [\mathrm{m}]} \tag{A.2}$$

where ρ_s and ρ_p are the general electrical concrete resistivity and polarization resistivity, c and d are the cover depth and diameter of steel which is placed near the concrete surface, respectively.

Based on the Ohm's law, there is:

$$\eta|_{x+dx} - \eta|_x = \rho_{s1} \cdot dx \cdot I_{f(x)} \tag{A.3}$$

where

$$\eta_x = E_{corr} - E_x \tag{A.4}$$

Meanwhile, based on Kirchhoff's current law, i.e. the current flowing into a certain element should be equal to the current flowing out of it:

$$I_f|_x - I_f|_{x+dx} = I_F \cdot dx = -\frac{\eta_x}{\rho_{p1}} \cdot dx \tag{A.5}$$

Consequently, the following equation can be obtained:

$$\frac{d\eta}{dx}\Big|_{x+dx} - \frac{d\eta}{dx}\Big|_x = \rho_{s1} \cdot \frac{\eta_x}{\rho_{p1}} \cdot dx \tag{A.6}$$

i.e.

$$\frac{d^2\eta_x}{dx^2} = \frac{\rho_{s1}}{\rho_{p1}} \cdot \eta_x \tag{A.7}$$

The common solution of Eq. (A.7) is expressed as Eq. (5).

References

Alhozaimy, A., Hussain, R. R., Al-Zaid, R. and Negheimish, A. Al (2012) 'Investigation of severe corrosion observed at intersection points of steel rebar mesh in reinforced concrete construction', Construction and Building Materials. Elsevier Ltd, 37, pp. 67–81. doi: 10.1016/j.conbuildmat.2012.07.011.

Altun, H. and Sen, S. (2004) 'Studies on the influence of chloride ion concentration and pH on the corrosion and electrochemical behaviour of AZ63 magnesium alloy', Materials and Design, 25, pp. 637–643. doi: 10.1016/j.matdes.2004.02.002.

Andrade, C., Maribona, I. R., Feliu, S., González, J. A. and Feliu, S. (1992) 'The effect of macrocells between active and passive areas of steel reinforcements', Corrosion Science, 33(2), pp. 237–249. doi: 10.1016/0010-938X(92)90148-V.

Angst, U. M., Geiker, M. R., Michel, A., Gehlen, C., Wong, H., Isgor, O. B., Elsener, B., Hansson, C. M., François, R., Hornbostel, K., Polder, R., Alonso, M. C., Sanchez, M., Correia, M. J., Criado, M., Sagüés, A. and Buenfeld, N. (2017) 'The steel–concrete interface', Materials and Structures, 50(2), p. 143. doi: 10.1617/s11527-017-1010-1.

Bazant, Z. P. (1979a) 'Physical Model for Steel Corrosion in Concrete Sea Structures-Theory', Journal of the Structural Division, 105(June).

Bazant, Z. P. (1979b) 'Physical model for steel corrosion in concrete sea structures - application', Journal of the Structural Division-ASCE, 105(6), pp. 1154–1166.

DuraCrete (2000) 'General Guidelines for Durability Design and Redesign', The European Union-Brite Euram III, Project No. BE95-1347, Probabilistic Performance -based Durability Design of Concrete Structures, pp. 1–138.

Fu, C., Jin, N., Ye, H., Jin, X. and Dai, W. (2017) 'Corrosion characteristics of a 4-year naturally corroded reinforced concrete beam with load-induced transverse cracks', Corrosion Science. Elsevier Ltd, 117, pp. 11–23. doi: 10.1016/j.corsci.2017.01.002.

Guidelines, G. and Design, D. (2000) 'DuraCrete - Final Technical Report'.

Hansson, C. M., Poursaee, A. and Laurent, A. (2006) 'Macrocell and microcell corrosion of steel in ordinary Portland cement and high performance concretes', Cement and Concrete Research, 36(11), pp. 2098–2102. doi: 10.1016/j.cemconres.2006.07.005.

Hornbostel, K., Angst, U. M., Elsener, B., Larsen, C. K. and Geiker, M. R. (2016) 'Influence of mortar resistivity on the rate-limiting step of chloride-induced macro-cell corrosion of reinforcing steel', Corrosion Science. Elsevier Ltd, 110, pp. 46–56. doi: 10.1016/j.corsci.2016.04.011.

Huet, B., L'hostis, V., Santarini, G., Feron, D. and Idrissi, H. (2007) 'Steel corrosion in concrete: Determinist modeling of cathodic reaction as a function of water saturation degree', Corrosion Science, 49(4), pp. 1918–1932. doi: 10.1016/j.corsci.2006.10.005.

Izquierdo, D., Alonso, C., Andrade, C. and Castellote, M. (2004) 'Potentiostatic determination of chloride threshold values for rebar depassivation - Experimental and statistical study', Electrochimica Acta, 49(17–18), pp. 2731–2739. doi: 10.1016/j.electacta.2004.01.034.

Ji, Y. S., Zhao, W., Zhou, M., Ma, H. R. and Zeng, P. (2013) 'Corrosion current distribution of macrocell and microcell of steel bar in concrete exposed to chloride environments', Construction and Building Materials. Elsevier Ltd, 47, pp. 104–110. doi: 10.1016/j.conbuildmat.2013.05.003.

Laidler, K. J. (1970) 'The kinetics of electrode processes', Journal of Chemical Education, 47(9), p. 600. doi: 10.1021/ed047p600.

Lewis, D. A. and Copenhagen W J. (1959) ' Corrosion of Reinforcing Steel in Concrete in Marine Atmospheres★' , Corrosion, 15(7), pp. 60‒66.

Liu, T. and Weyers, R. . (1998) 'Modeling the Dynamic Corrosion Process in Chloride Contaminated Concrete Structures', Cement and Concrete Research, 28(3), pp. 365–379. doi: 10.1016/S0008-8846(98)00259-2.

Moreno, M., Morris, W., Alvarez, M. G. and Duff, G. S. (2004) 'Corrosion of reinforcing steel in simulated concrete pore solutions Effect of carbonation and chloride content', 46, pp. 2681–2699. doi: 10.1016/j.corsci.2004.03.013.

Otieno, M., Beushausen, H. and Alexander, M. (2016) 'Chloride-induced corrosion of steel in cracked concrete - Part II: Corrosion rate prediction models', Cement and Concrete Research. Elsevier Ltd, 79, pp. 386–394. doi: 10.1016/j.cemconres.2015.08.008.

Pack, S., Jung, M., Song, H., Kim, S. and Ann, K. Y. (2010) 'Prediction of time dependent chloride transport in concrete structures exposed to a marine environment', Cement and Concrete Research. Elsevier Ltd, 40(2), pp. 302–312. doi: 10.1016/j.cemconres.2009.09.023.

Pech-Canul, M. A. and Castro, P. (2002) 'Corrosion measurements of steel reinforcement in concrete exposed to a tropical marine atmosphere', Cement and Concrete Research, 32(3), pp. 491–498. doi: 10.1016/S0008-8846(01)00713-X.

Qian, S., Zhang, J. and Qu, D. (2006) 'Theoretical and experimental study of microcell and macrocell corrosion in patch repairs of concrete structures', Cement and Concrete Composites, 28(8), pp. 685–695. doi: 10.1016/j.cemconcomp.2006.05.010.

Song, G. L. (2010) 'Potential and current distributions of one-dimensional galvanic corrosion systems', Corrosion Science. Elsevier Ltd, 52(2), pp. 455–480. doi: 10.1016/j.corsci.2009.10.003.

Tahara, A. and Kodama, T. (2000) 'Potential distribution measurement in galvanic corrosion of Zn/Fe couple by means of Kelvin probe', Corrosion Science, 42(4), pp. 655–673. doi: 10.1016/S0010-938X(99)00074-8.